

Mechanical properties of transparent sodium phosphosilicate glass-ceramics

Qi Zhang,¹ Rasmus Christensen,¹ Mikkel L. Bødker,¹ Tao Du,¹ Theany To¹,¹ Francisco Muñoz^{2,*},
Mathieu Bauchy,³ and Morten M. Smedskjaer^{1,†}

¹*Department of Chemistry and Bioscience, Aalborg University, 9220 Aalborg, Denmark*

²*Institute of Ceramics and Glass (CSIC), 28049 Madrid, Spain*

³*Department of Civil and Environmental Engineering, University of California, Los Angeles, California 90095, USA*



(Received 28 January 2023; revised 26 April 2023; accepted 12 June 2023; published 30 June 2023)

Glass-ceramics feature excellent mechanical properties but tend to lack transparency due to the presence of large crystals with a different refractive index from the matrix glass. Here, we investigate the relationship between the heterogeneous microstructure, mechanical properties (hardness, crack resistance, and fracture toughness), and transparency in $\text{Na}_2\text{O}-\text{P}_2\text{O}_5-\text{SiO}_2$ glass-ceramics. The mechanical properties are determined by the combination of crystal type, content, and size, as well as the remaining glass-matrix structure. The crystal fraction and size increase upon heat treatment, whereas the network connectivity of the residual glass-matrix phase decreases. These observed changes have opposite effects on crack resistance and fracture toughness. Changes in crystallization behavior have a more significant effect on crack resistance relative to that on fracture toughness, while changes in crystal size have a more pronounced effect on fracture toughness. The glass-ceramic samples feature excellent transmittance and reach a maximum fracture toughness of $1.1 \text{ MPa m}^{0.5}$.

DOI: [10.1103/PhysRevMaterials.7.063606](https://doi.org/10.1103/PhysRevMaterials.7.063606)

I. INTRODUCTION

Given their diverse application fields, there is a high demand for new oxide glass materials with improved strength and resistance to damage, while maintaining their transparency. As such, the brittleness of glass is the most critical obstacle towards many applications [1,2]. Glasses with improved elastic moduli, crack initiation resistance, or fracture toughness can be achieved through compositional design [3–5]. However, the homogeneous microstructure of glass makes it challenging to significantly decrease its brittleness through only compositional design, especially as the fracture toughness (K_{Ic}) typically plateaus around a maximum value slightly greater than $1 \text{ MPa m}^{0.5}$ for oxide glasses. As a result, various post-treatment methods have been attempted [6,7], for example relying on reinforcements to control the driving force at the crack tip. As an attractive alternative, partial crystallization of glasses to form so-called glass-ceramics has attracted extensive attention for their excellent mechanical properties compared to their parent glasses [8,9].

Glass-ceramics are produced through controlled formation of one or more crystalline phases embedded in a glassy matrix via nucleation and growth processes. The generation of crystal inclusions in the glass matrix can have an impact on the mechanical properties of the material. For example, previous work has found that glass-ceramics with higher crystal volume fraction tend to exhibit higher fracture toughness due to toughening mechanisms such as crack deflection, multiple cracking, crack bridging, and crack branching operated

at the crack tip [10]. Moreover, the crystal size and shape also affect fracture toughness [11–13]. However, the crystallization usually causes residual stresses due to the thermal expansion mismatch between the crystal and the glass matrix, which also influences properties such as crack-initiation resistance [10,14]. Meanwhile, the mechanical properties of glass-ceramics are not only affected by the crystals (content, size, shape, etc.), but also by the properties of the residual glass matrix. Some studies show that glass phases with large free volume or with self-adaptive networks can feature high crack-initiation resistance since energy dissipation can easily occur through the densification process, whereas glass structures with dense network connectivity and strong bonds can feature higher fracture toughness [4,15,16]. The composition and structure of the residual glass matrix changes upon crystallization (besides the case of isochemical crystallization) and these effects on the mechanical properties of glass-ceramics also need to be considered. As such, the mechanical properties of glass-ceramics will be determined by both the crystal and residual glass-matrix phases. In addition, the higher crystal content or large crystal size will generally decrease the transmittance of the glass-ceramics [17,18]. More work is therefore needed to improve our understanding of the link between the glass network structure, crystallization, and the mechanical properties of oxide glass-ceramics, and ultimately design tough, yet transparent glass-ceramics.

In this work, we focus on sodium phosphosilicate ($\text{Na}_2\text{O}-\text{P}_2\text{O}_5-\text{SiO}_2$) nanoglass-ceramics. When P_2O_5 is added to the $\text{Na}_2\text{O}-\text{SiO}_2$ system, it tends to cause phase separation in the glass and consume nonbridging oxygens from the silicate network to form $3\text{Na}^+ \text{PO}_4^{3-}$ -like complexes, which in turn induces repolymerization of the silicate glass structure [19–22]. Phase separation is believed

*fmunoz@icv.csic.es

†mos@bio.aau.dk

TABLE I. Nominal/target chemical compositions (in mol. %) and properties of as-prepared glass-ceramic samples, including Y parameter (see Sec. III B), glass-transition temperature (T_g), glass-softening temperatures (T_d), density (ρ), Young's modulus (E), and Poisson's ratio (ν). T_g has been determined using both DSC and dilatometry. Errors in T_g , ρ , E , and ν do not exceed ± 3 K, 0.01 g cm $^{-3}$, 2 GPa, and 0.01 , respectively.

Sample ID	Na ₂ O	SiO ₂	P ₂ O ₅	Y parameter	DSC		Dilatometry		ρ (g cm $^{-3}$)	E (GPa)	ν
					T_{g1} (K)	T_{g2} (K)	T_g (K)	T_d (K)			
NSP-1	45	44	11	3.45	586	726	828	990	3.10	67	0.23
NSP-2	50	40	10	3.00	517	723	784	898	3.16	67	0.25
NSP-3	50	45	5	2.44		691	702	759	3.15	65	0.26

to be a precursor of crystallization in many systems [23,24]. Li *et al.* discovered transparent Na₂O–Al₂O₃–SiO₂–P₂O₅ glass-ceramics with the Na₃PO₄ crystalline phase [25]. Hence, the Na₂O–P₂O₅–SiO₂ ternary system glass may be a good model that could contain only the Na₃PO₄ crystal with the possibility to make transparent glass-ceramics and tailor the mechanical properties through composition design and heat treatment. The purpose of this work is thus to investigate the effect of residual glass-matrix structure, crystal content, and crystal size on the mechanical properties of Na₂O–P₂O₅–SiO₂ glass-ceramics. To this end, we have prepared three transparent sodium phosphosilicate glasses with Na₃PO₄ crystals. Here, we directly obtain crystallized glass-ceramics samples through the melt-quenching process, but also perform subsequent heat treatment to further vary the crystal content and size. We then investigate the resulting changes in the network structure of the residual glass matrix as well as the mechanical properties, including hardness, crack-initiation resistance, and fracture toughness.

II. METHODS

A. Sample preparation

The sodium phosphosilicate samples were synthesized by melting a homogeneous mixture of reagent-grade Na₂CO₃, SiO₂, and NH₄H₂PO₄ in an alumina crucible in air at 1623 K for 2 h. To facilitate the ²⁹Si solid-state NMR spectroscopy measurements by reducing the relaxation times, we also doped the melts with 0.2 mol. % MnO. The nominal compositions of the samples (mol. %) are shown in Table I and are named NSP-1, NSP-2, and NSP-3, and the analyzed glass compositions as determined using x-ray fluorescence are shown in Supplemental Material, Table S1 [26]. Network formers form strong covalent bonds with oxygen to create the glass framework, while network modifiers occupy the voids in the glass network and modify them by forming weaker ionic bonds with oxygen. In this work, SiO₂ and P₂O₅ are the network former oxides, and Na₂O is the network modifier oxide. For NSP-1 and NSP-2, the ratio of SiO₂ to P₂O₅ is kept at 4:1, while the ratio of modifier to former oxides is 1:1.22 for NSP-1 and 1:1 for NSP-2. For NSP-3, the ratio of modifier to former is 1:1, but the content of SiO₂ is increased to 45 mol. %, and the content of P₂O₅ is decreased to 5 mol. %. These composition changes were made to directly synthesize glass-ceramics with only one type of crystal and investigate

the mechanical properties of samples obtained upon different crystallization conditions.

After homogenization, the melts were quenched on a stainless-steel plate to obtain bulk melt-quenched samples that were transferred to an annealing furnace at their estimated glass-transition temperature (T_g) (523 K for NSP-1, 482 K for NSP-2, and 623 K for NSP-3) and cooled down to room temperature at a rate of 5 K min $^{-1}$. Small specimens of each glass were cut to measure the actual T_g value of each sample (see Sec. II C). The samples were reannealed at their measured respective T_g values. Using differential scanning calorimetry (DSC), we observed two glass-transition temperatures for NSP-1 and NSP-2, which are indicative of phase separation (see discussion in Sec. III C). To prevent more crystal formation, we chose the annealing temperatures as T_{g1} for NSP-1 and NSP-2, and T_{g2} for NSP-3. Moreover, the as-prepared samples were heat treated at $1.05T_{g1}$ (scaled in Kelvin) for 1 h to explore the effect of varying crystal content and size.

B. Structural characterization

The crystalline phases in the samples before and after heat treatment were identified by x-ray-diffraction (XRD) analysis (Empyrean XRD, PANalytical) with a monochromator Cu $K\alpha$ radiation (1.5406 Å). XRD patterns were acquired in the range from 10° to 70° at 40 kV with a scanning speed of 8° min $^{-1}$. To quantify the change of crystalline content upon the heat treatment at $1.05T_g$, we included corundum (α -Al₂O₃) as a reference material during the XRD testing. That is, we ground and mixed 0.85-g glass-ceramic sample with 0.15-g corundum powder, which was used as the XRD test samples.

The ³¹P magic-angle spinning (MAS) NMR spectra were recorded on a Bruker 400-MHz spectrometer (9.4 T) at 161.96 MHz with a spinning speed of 10 kHz. The acquisition was done using $\pi/2$ pulses of 60 kHz, with a total number of 128 scans and a recycle delay (rd) of 40 s. (NH₄)₂PO₄ was used as a reference, at 0.81 ppm with respect to H₃PO₄ (85%). The ²⁹Si MAS NMR spectra were recorded at 79.52 MHz using a 4-mm probe at a spinning rate of 10 kHz and $\pi/2$ pulses with an rd time of 240 s. Kaolinite was employed as the chemical-shift reference, at -91.2 ppm with respect to standard tetramethylsilane (TMS). NMR spectra were simulated using DMFIT software [27].

The phase morphology of the quenched and heat-treated glass-ceramic samples was investigated using a field-emission scanning electron microscope (SEM) (Zeiss Cross Beam) at an acceleration voltage of 10 kV. All samples were gold coated before testing, but no etching was performed. The size

distribution of the crystal phase was analyzed based on the SEM images using the IMAGEJ software.

C. Properties characterization

The glass-transition temperature (T_g) of the as-prepared and heat-treated samples was determined using DSC (STA 449 F1, Netzsch). We used samples polished down to a thickness of 1 mm. These were tested in alumina crucibles under a flow of argon (gas flow 40 mL min⁻¹). The heating rate was 10 K min⁻¹, and after reaching the final temperature, cooled down to room temperature with a cooling rate of 20 K min⁻¹. The intercept between the tangent to the inflection point of the endothermic peak and the extrapolated heat flow of the glass was interpreted as the T_g . Based on the repeated measurements of T_g on other glasses in our laboratory using the same procedure, the error in the determined T_g value is estimated to be around ± 3 K. Glass-transition and dilatometric-softening temperatures were also estimated from dilation curves obtained in a Netzsch Gerätebau dilatometer, model 402 PC/1, at a heating rate of 5 K min⁻¹. Measurements were done on prismatic samples of ~ 10 mm in length from as-prepared glasses, using Al₂O₃ as the calibration standard.

The density (ρ) of the glass-ceramic samples was tested using Archimedes' principle of buoyancy at room temperature (~ 295 K). The samples (1.5 g) were tested ten times in air and ethanol, and the density value was the average of the ten results. The elastic properties of the glasses were measured by ultrasonic echography using an ultrasonic thickness gauge (38DL Plus, Olympus) equipped with 20-MHz delay line transducers to determine the longitudinal (V_1) and transversal (V_2) wave velocities. The longitudinal modulus C_{11} , shear modulus G , bulk modulus B , and Young's modulus E , as well as the Poisson ratio ν were calculated using the relationship formulas for isotropic materials [28]. The detailed results of the ultrasonic echography measurements are shown in Supplemental Material, Table S2 [26].

Vickers hardness (H_V) and crack-initiation resistance (CR) of the samples were determined by using a Nanovea CB500 hardness tester. The glass specimens were polished in ethanol using SiC paper with decreasing abrasive particle size (up to grit 4000), followed by polishing in a water-free 1- μ m diamond suspension. A Vickers indenter tip (four-sided pyramid-shaped diamond with an angle of 136°) was used to perform the indentations. All indentations were conducted at room temperature (~ 295 K) and relative humidity of $29 \pm 4\%$. Twenty indents were performed for each specimen at a load of 0.49 N applied for 10 s to determine H_V values, which were calculated as $H_V = 1.8544P/d^2$, with P being the contact load and d the average length of the residual indent diagonals. According to the method of Wada *et al.* [29], the probability of crack initiation is defined as the ratio between the number of corners with cracks and the total number of corners on all indents (i.e., four corners for Vickers indenter). CR was determined as the load at which the crack probability is 50%. To calculate CR , each glass specimen was indented 30 times at different loads, increasing in steps from 0.1 to 6 N with loading duration of 15 s and dwell time of 10 s. Then, the number of corner cracks was counted at each load to determine CR from the crack probability vs load curve.

Fracture toughness (K_{Ic}) was determined using the single-edge precrack beam (SEPB) method at room temperature (~ 295 K) and relative humidity of $29 \pm 4\%$, following the well-established procedure [30,31]. Five polished glass beams with dimensions of about $1.5 \times 2 \times 10$ mm³ were prepared for each as-prepared and heat-treated sample. Eight Vickers indents with a load of 4.9 N for a dwell time of 5 s were placed on a line on the breadth side ($B = 1.5$ mm), and the indented samples were stored in absolute ethanol to exclude the air. As the next step, the indented specimen was positioned in a bridge-compressive fixture with a groove size of approximately 3 mm (1.5 times the specimen width, $W = 2$ mm) to produce a precrack with a cross-head speed of 0.02 mm min⁻¹. The indented side of the specimen (the lower part) experienced tensile stress, whereas the other side experienced compressive stress. A crack was initiated from the indent corners under the tensile stress, and then propagated until it reached the middle of the specimen width, where the compressive stress exists. Afterward, the precracked specimen was quickly positioned in a three-point bending fixture and the specimen was fractured with a cross-head speed of 10 μ m s⁻¹ to minimize humidity effects [32,33]. After the fracture, the precrack length (a) was obtained as the average of three precrack lengths measured at various fractions (25, 50, and 75%) of the breadth side. The adapted three-point bending span (S) of about 8 mm was designed to fulfill the span-to-width ratio of, at least, about 4 to avoid the span-length dependence. K_{Ic} was then calculated from the peak load (P_{max}),

$$K_{Ic} = \frac{P_{max}}{B\sqrt{W}} Y^*, \text{ where } Y^* = \frac{3}{2} \frac{S}{W} \frac{\alpha^{1/2}}{(1-\alpha)^{3/2}} f(\alpha), \quad (1)$$

where α is the precrack-width ratio (a/W) and $f(\alpha) = [1.99 - (\alpha - \alpha^2)(2.15 - 3.93\alpha + 2.7\alpha^2)] / (1 + 2\alpha)$. The average K_{Ic} value was calculated from the results of five valid tests. More details on the methods can be found elsewhere [31,32].

Ultraviolet-visible (UV-vis) spectroscopy (Cary 50 Bio, Varian) was used to determine the optical transparency of as-prepared and heat-treated samples. The wavelength range of the transmission spectrum was set to 200–800 nm. Around 1.5-mm-thick polished samples were used for the tests, but we note that all the presented UV-vis transmittance spectra were normalized to a thickness of 1 mm.

D. Simulation of the properties of Na₃PO₄ crystal

Since no data on the properties of the Na₃PO₄ crystal could be found in literature, we simulated its elastic properties with the LAMMPS software using the recently published BMP-harm (where BMP is Bertani-Menziani-Pedone) interatomic potential [34]. The BMP-harm potential is based on the PMMCS (Pedone-Malavasi-Menziani-Cormack-Segre) potential [35], where two-body terms are handled using a long-range Coulombic interaction combined with a short-range Morse function and a repulsive interaction of the form B_{ij}/r^{12} as seen in Eq. (2):

$$U_{ij}(r_{ij}) = \frac{z_i z_j e^2}{r_{ij}} + D_{ij} \left(\left\{ 1 - \exp[-a_{ij}(r_{ij} - r_{ij}^0)] \right\}^2 - 1 \right) + \frac{B_{ij}}{r_{ij}^{12}}. \quad (2)$$

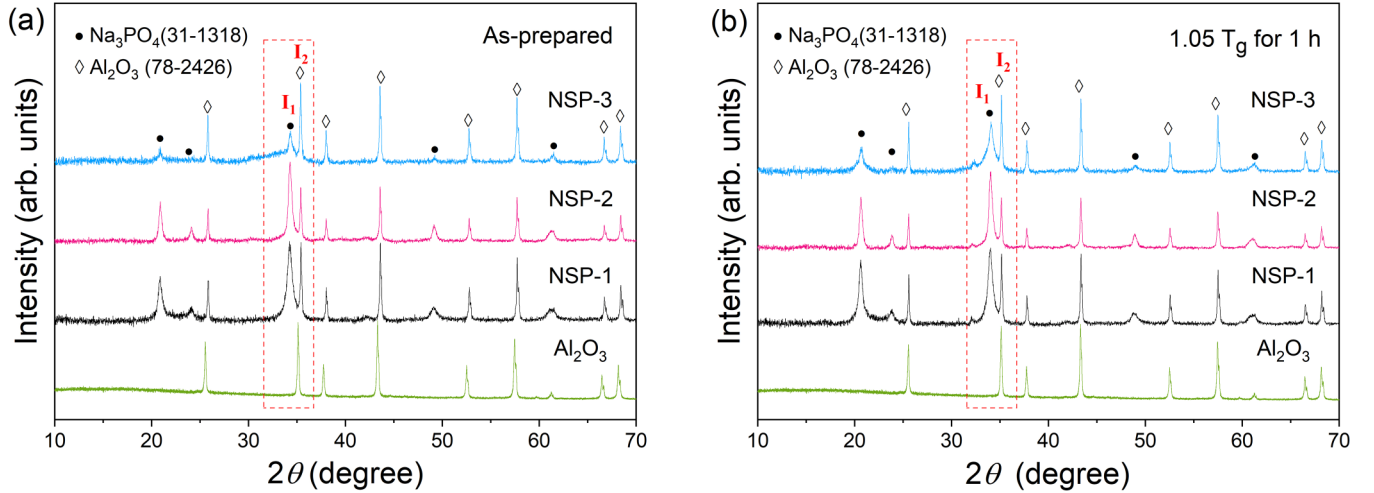


FIG. 1. XRD patterns of glass-ceramic samples with a mixture of corundum powders as reference. (a) As-prepared glass-ceramic samples. (b) Glass-ceramic samples after heat treatment at $1.05T_g$ for 1 h. XRD pattern of corundum (α - Al_2O_3 , ICDD Card No. 78–2426) is also included for comparison.

Here, z_i is the partial charge of atom i ; D_{ij} , a_{ij} , and r_{ij}^0 are parameters of the Morse function; and B_{ij} is the parameter for the repulsive interaction for the pair of atoms i and j .

The BMP-harm potential further expands on this potential, handling the repulsive interactions between phosphorous atoms using a Buckingham function ($A_{ij}e^{-r_{ij}/\rho_{ij}}$) and employing a three-body term for the P-O-P angle through a simple harmonic functional form as seen in Eq. (3):

$$U(\theta_{\text{POP}}) = \frac{k_{\text{POP}}}{2} (\theta_{\text{POP}} - \theta_{\text{POP},0})^2. \quad (3)$$

Here, k_{POP} and $\theta_{\text{POP},0}$ are the force constant and reference angle for the P-O-P angle. Values for the potential parameters can be found in Ref. [34]. The initial Na_3PO_4 crystal structure was taken from the literature [36], where we note that γ - Na_3PO_4 is a cubic crystal with the space group $Fm\bar{3}m$. The crystal structure was replicated four times in all directions to form a $4 \times 4 \times 4$ supercell.

First, potential-energy minimization of the initial structure was performed. Thereafter, elastic constants were obtained by subjecting the structures to stepwise elongations and compressions of $\varepsilon = 0.0001 = 0.01\%$ in the tensile directions xx , yy , and zz as well as in the shear directions xy , xz , and yz . After each deformation step, the potential energy of the structure was minimized, and the measured stress in all directions was recorded. Ten elongations and compressions were performed in each direction. After recording the stress-strain curves, a linear regression was performed to obtain the elastic constants of the systems. Six repetitions of the simulation were performed to ensure proper statistics. Voigt-Reuss-Hill [37] averages were used to calculate the polycrystalline moduli of the crystal. The stress-strain curves are shown in Supplemental Material, Fig. S1 [26].

III. RESULTS

A. Phase microstructure analysis

Figures 1(a) and 1(b) are the XRD patterns of as-prepared and heat-treated glass-ceramic samples, respectively.

The XRD pattern of corundum (α - Al_2O_3 , International Centre for Diffraction Data (ICDD) Card No. 78–2426) is also included for comparison. The patterns have been normalized by the intensity of the strongest peak. All as-prepared specimens have been crystallized during the melt-quenching and/or annealing procedures, as shown in Fig. 1(a). Na_3PO_4 (ICDD Card No. 31–1318) is the main crystal phase in both the as-prepared and heat-treated glass-ceramics. By comparing the diffraction intensity of Na_3PO_4 ($2\theta = 33.9^\circ$, referred to as I_1) and α - Al_2O_3 ($2\theta = 35.1^\circ$, referred to as I_2), we find the I_1/I_2 ratio in as-prepared samples to be 1.015, 1.474, and 0.394 for NSP-1, NSP-2, and NSP-3 compositions, respectively. After heat treatment at $1.05T_g$ for 1 h, the ratio increases to 1.087, 1.526, and 0.651, respectively. The crystallinity of the NSP-2 composition is the highest for both the as-prepared and heat-treated samples. Although the crystallinity of NSP-3 is the lowest for both the as-prepared and heat-treated samples, the I_1/I_2 ratio of NSP-3 increases the most after heat treatment (by approximately 65%). The XRD results reveal that both NSP-1 and NSP-2 have a relatively high content of crystals before and after the heat treatment, but the heat treatment has a smaller effect on the increase of crystallinity relative to that in NSP-3. This effect is determined by the chemical composition and residual glass structure, as will be explained in detail in Sec. IV, Discussion.

Figure 2 shows the InLens morphology and size distribution of the crystal phase in the as-prepared and heat-treated samples. The crystal size distributions in the different samples are shown in Supplemental Material, Fig. S2 [26]. Considering that only one type of crystal (Na_3PO_4) is presented in all the samples according to the XRD results, the white regions can be assigned to this crystal phase, whereas the dark regions represent the residual glass-matrix phase. For the as-prepared NSP-1 sample, the average size of the crystal phase is around 47 nm, and the crystals are distributed homogeneously throughout the glass matrix [Fig. 2(a)]. After heat treatment, more white regions appear, and the average size of the crystal increases up to 83 nm, although we note that there are still some crystals present with sizes in the range < 50 nm.

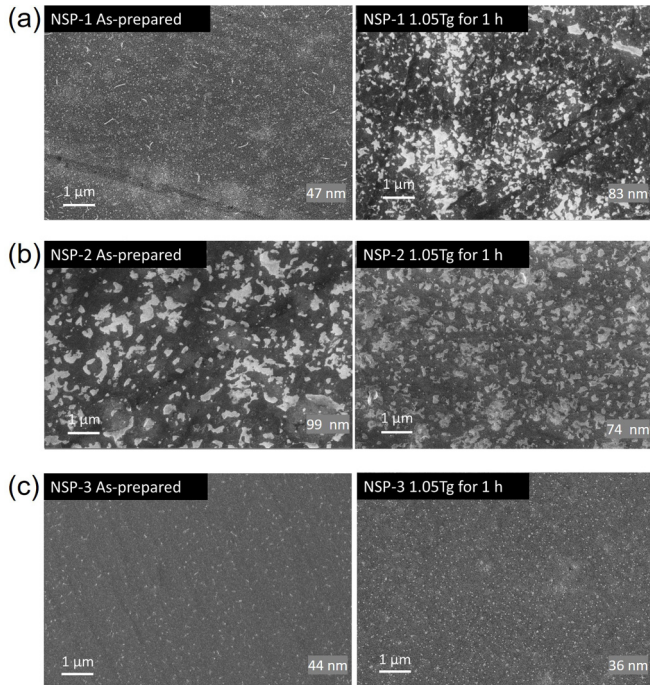


FIG. 2. SEM morphology and average size of crystal phase in as-prepared and heat-treated samples: (a) NSP-1, (b) NSP-2, and (c) NSP-3.

Figure 2(b) shows the morphology of NSP-2 samples, with the average crystal size decreasing from around 99 to 74 nm upon heat treatment. However, the amount of crystals increases and the crystal distribution appears more homogeneous in the heat-treated NSP-2 sample. For the NSP-3 as-prepared sample

[Fig. 2(c)], the glass matrix is dominant, and the average size of the crystal is around 44 nm. Upon heat treatment, the amount of the crystals increases significantly and the average size decreases slightly to around 36 nm. By combining the SEM and XRD results analysis, we find an interesting phenomenon. Namely, although the crystal content of NSP-1 changes only to a small extent after heat treatment, the heat treatment effectively promotes the growth of the crystal size. In contrast, for NSP-3, although the crystal content increases markedly after heat treatment, the crystal size features no significant change. For NSP-2, the effect of heat treatment on both crystallinity and crystal size is not obvious.

B. Glass-ceramics network structure

Figure 3(a) shows the ^{31}P MAS NMR spectra of the as-prepared and heat-treated samples. In the spectrum of glass sample NSP-1, two main resonances can be seen at approximately 13 and 2 ppm that are assigned to monomeric (PO_4^{3-}) and dimeric ($\text{P}_2\text{O}_7^{4-}$) units, respectively [38,39]. Both signals were simulated using Gaussian/Lorentzian curves, being mainly Lorentzian in shape. The lower field signal appears at 13.7 ppm, 2.87 ppm in width, and it therefore corresponds to the ordered arrangement of phosphorus in sodium orthophosphate crystalline phase [40,41]. Similarly, very minor amounts of phosphorus nuclei in a different environment and relatively disordered in nature could be detected by NMR from the small and broad resonance that can be seen centered at 1.84 ppm. The ^{31}P NMR of crystalline sodium pyrophosphate ($\text{Na}_4\text{P}_2\text{O}_7$) would produce a doublet between 2 and 3 ppm, values which are close to the observed minor resonances in NSP-1 spectra [42]. It is thought that

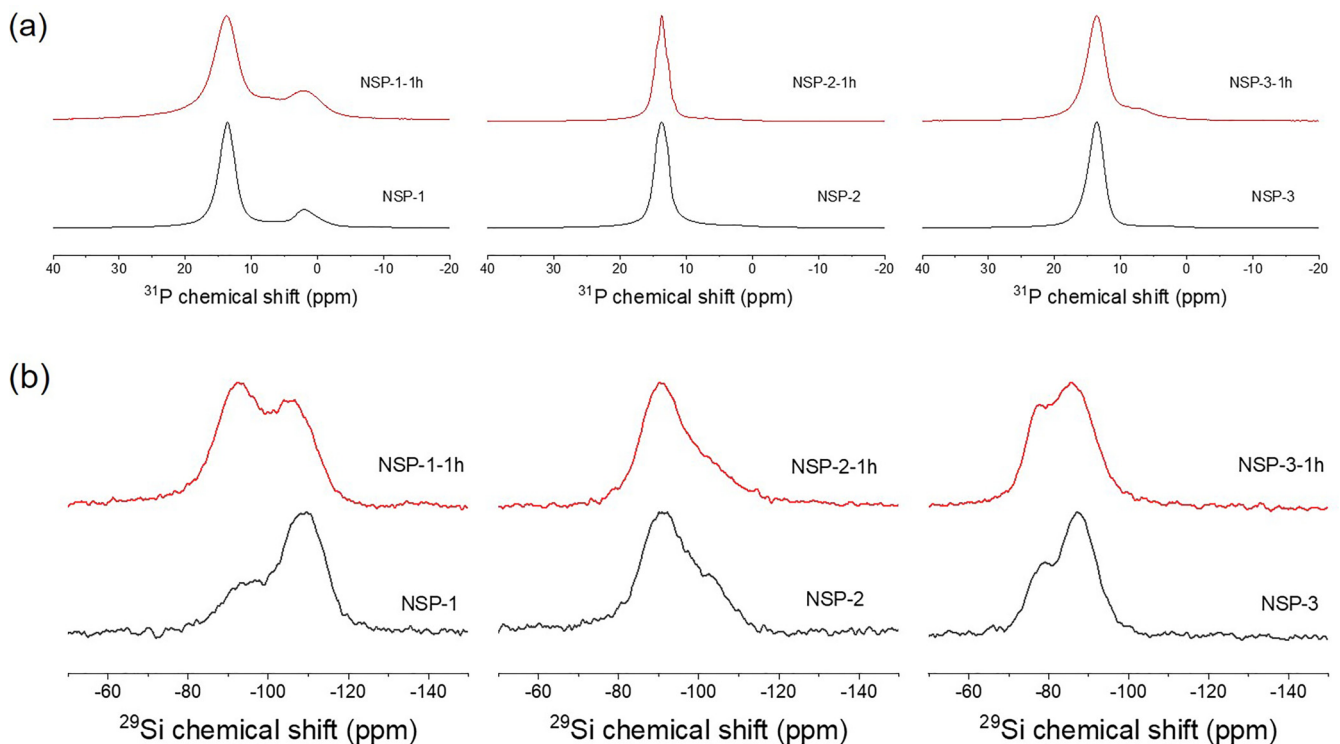


FIG. 3. MAS NMR spectra of studied glass-ceramics before and after 1-h heat treatment: (a) ^{31}P and (b) ^{29}Si .

some phosphorus may have condensed into $(P_2O_7)^{4-}$ dimers, although remaining in a higher amorphous character than the one producing Na_3PO_4 crystals as confirmed by XRD. Thermal treatment of sample NSP-1 gives rise to a similar NMR spectrum in sample NSP-1-1h, although a small third component appearing at about 7.5 ppm should be taken into account and is thought to arise from some sort of hydrated Na_3PO_4 phase [42]. Based on the ^{31}P NMR and XRD results, P is found to mainly be present as Na_3PO_4 phase in all the glass-ceramic samples. NSP-2 and NSP-3 samples show mainly the resonance attributed to phosphorus in Na_3PO_4 and thermal treatment does not produce important modifications of the phosphorous environment, except some small contribution at about 7 ppm for NSP-3-1h which is not anyway reflected in the XRD patterns.

The main network former in the present samples is SiO_2 , i.e., the connectivity of the silicate network plays a critical role for the mechanical properties of the glass-ceramics. Stevels *et al.* have proposed to evaluate the network connectivity of glasses through the so-called Y parameter [43]. The degree of polymerization of glasses is determined by the concentration of network modifiers, and the Y (Si) parameter describes the number of bridging oxygen (BO) atoms per silicate tetrahedron. It can be calculated from the molar composition of the glasses as $Y = 2Z - 2R$, where Z is the average number of all types of oxygen per polyhedron ($Z = 4$ for Si tetrahedron), and R is the ratio of the total number of oxygen atoms to the total number of glass-forming cations [44]. The ^{31}P NMR results show that P_2O_5 is mainly present as orthophosphate species with Na^+ cations required to maintain charge balance. Therefore, the silicate connectivity (Y parameter) is calculated assuming all P_2O_5 in glass is present as orthophosphate (Na_3PO_4), i.e., we deduct the oxygen atoms used to form Na_3PO_4 from the total number of oxygen atoms,

$$Y = 2 \times 4 - 2 \times \frac{(Na_2O + 2 \times SiO_2 + 5 \times P_2O_5 - 4 \times 2 \times P_2O_5)}{SiO_2}. \quad (4)$$

The Y parameter for each composition is shown in Table I, with values of 3.45, 3.00, and 2.44 for NSP-1, NSP-2, and NSP-3, respectively. This indicates a decrease in the connectivity of the glass matrix in glass-ceramics from NSP-1 to NSP-3.

Figure 3(b) shows the ^{29}Si MAS NMR spectra of the as-prepared and heat-treated samples. The silicate glass structure units can be classified by the Q^n ($n = 0, 1, 2, 3, \text{ or } 4$) notation, where n refers to the number of BO per structure unit tetrahedron [45]. The ^{29}Si MAS NMR spectra of binary sodium silicate glasses consist of the four peaks at around $-69, -77, -90$ and -100 ppm, which are assigned to the Si (Q^1), Si (Q^2), Si (Q^3), and Si (Q^4) units, respectively [46]. However, the chemical shifts of Si (Q^n) in P_2O_5 -rich glasses are more negative than those observed in binary alkali silicate glasses [46,47]. In a sodium phosphosilicate glass ($34.5Na_2O - 55.5P_2O_5 - 10SiO_2$), a very faint peak at ~ -120 ppm has previously been assigned to Si (Q^4) [48]. Thus, in this work, the ^{29}Si NMR spectra consist of the three peaks at around $-75, -85, \text{ to } -95$ and $-100, \text{ to } -110$ ppm, which can be assigned to Si (Q^2), Si (Q^3), and Si (Q^4) units, respectively.

From the ^{29}Si MAS NMR spectra of samples, the relative intensity of the signals at more positive chemical shifts for heat-treated samples increases. That is, in the Si-O network, the content of Si (Q^2) and Si (Q^3) units increases compared to the content of Si (Q^4) unit. In turn, this indicates that the content of bridging oxygen in the Si-O network decreases and the densification degree of $[SiO_4]$ tetrahedral decreases upon heat treatment. Table II summarizes the deconvolution results of silicate speciation and the calculated number of nonbridging oxygen (NBO) per SiO_4 tetrahedron (T).

NBO/T has been calculated from the Si(Q^n) percentages determined by ^{29}Si MAS-NMR [40],

$$NBO/T_{(^{29}SiNMR)} = \left[\sum (\%Q_{Si}^n)_{NMR} (NBO/T)_n \right] / 100, \quad (5)$$

where $(NBO/T) = 4$ for Q^0 , $(NBO/T) = 3$ for Q^1 , $(NBO/T) = 2$ for Q^2 , $(NBO/T) = 1$ for Q^3 , and $(NBO/T) = 0$ for Q^4 . The NBO/T values for the as-prepared samples are found to be 0.32, 0.74, and 1.25 for NSP-1, NSP-2, and NSP-3, respectively, indicating reduced connectivity from NSP-1 to NSP-3. The experimental connectivity derived from the NMR data (NBO/T value) is consistent with the calculated results from the glass compositions (Y parameter), i.e., the Si-O network connectivity of as-prepared samples is determined by the composition and the ratio of O/Si. After heat treatment at $1.05T_g$ for 1 h, the NBO/T of NSP-1 and NSP-3 significant increases to 0.58 and 1.33, respectively, but NBO/T for NSP-2 does not appear to have clear change due to the broadness and low resolution of the spectra. Considering the changes in spectra and NBO/T, the polymerization degree of the glass matrix decreases upon heat treatment due to the decrease in NBO fraction, and the heat treatment has the most pronounced effect on the Si-O network of NSP-1, followed by NSP-3. However, NSP-1 maintains the highest polymerization degree of Si-O network before and after heat treatment, while NSP-3 has the lowest polymerization degree.

C. Glass characteristic temperature, density, and optical properties.

The glass-transition and glass-softening temperatures of the as-prepared glass-ceramic samples as well as the density results are summarized in Table I. The density of the samples, determined using Archimedes' principle of buoyancy, is relatively constant at around 3.1 g cm^{-3} . We also found no significant change in density upon heat treatment. The DSC heating curves are shown in Supplemental Material, Fig. S3 [26]. Based on these DSC results, the NSP-1 and NSP-2 samples exhibit two distinct glass-transition temperatures, while NSP-3 only exhibits one glass-transition temperature. The T_{g1} of NSP-1 and NSP-2 are 586 and 517 K, respectively, while the T_{g2} of NSP-1 to NSP-3 are 726, 723, and 691 K, respectively. A previous study has reported that liquid-liquid phase separation is promoted in silicate glass as the P_2O_5 content increases [25]. In such silicate compositions, phosphorus is mainly present as orthophosphate segregated in the glass network, acting to promote phase separation and crystallization. Hence, considering the XRD and NMR results, the samples with higher P_2O_5 content (NSP-1 and NSP-2) likely contain some P-rich domains in the matrix. Since the bond energy of

TABLE II. ^{29}Si isotropic chemical shift, relative abundance of Q^n entities, and NBO/T values calculated from Eq. (5). Uncertainties for isotropic chemical shift and area fraction are ± 1 ppm and 1%, respectively, while uncertainty in NBO/T is on the order of ± 0.05 .

Sample ID	δ isotropic (ppm)				% Relative abundance				NBO/T
	Q^1	Q^2	Q^3	Q^4	Q^1	Q^2	Q^3	Q^4	
NSP-1			-94	-109	0	0	32	68	0.32
NSP-1-1h			-92	-107	0	0	58	42	0.58
NSP-2		-77	-91	-102	0	5	64	31	0.74
NSP-2-1h			-90	-103	0	0	71	29	0.71
NSP-3		-77	-87		0	25	75	0	1.25
NSP-3-1h		-76	-86		0	33	67	0	1.33

Si–O (799.6 kJ/mol) is much larger than that of the P–O bond (599.1 kJ/mol) [44], and the connectivity of SiO_2 is higher than that of P_2O_5 , the lower T_g (T_{g1}) should belong to the P-rich phase, while the higher one (T_{g2}) should belong to the Si-rich phase.

We have also used dilatometry to analyze the glass characteristic temperatures. For this method, we are only able to detect one glass-transition temperature for each sample, with the T_g values decreasing from 828 K of NSP-1 to 784 K of NSP-2, and finally to 702 K of NSP-3. Since the main glass-former composition is SiO_2 , this T_g can be assigned to Si-rich glass matrix. Meanwhile, the glass-softening temperature also decreases from 990 K of NSP-1 to 898 K of NSP-2, and finally to 759 K of NSP-3. The decrease of T_g and T_d can be ascribed to the decrease of the Si–O network connectivity (Y parameter) [49].

Figure 4(a) shows photographs of the polished glass-ceramic samples after heat treatment, revealing good optical transparency. The purple color is due to the Mn doping, specifically to Mn^{3+} ions [50]. That is, the absorption band centered at ~ 490 nm can be seen in the UV-vis transmittance spectra in all samples due to the absorption of Mn^{3+} ions [50]. To

quantify the differences in transparency, Fig. 4(b) shows the measured UV-vis transmittance spectra of the glass-ceramics. The transmittance of three glass-ceramics in the wavelength region of visible light exceeds 80%. There is almost no change in transmittance upon heat treatment, with very high transmittance above 90% for all as-prepared samples at 800-nm wavelength. After heat treatment, the transmittance decreases slightly to 85% for NSP-1 and NSP-2 at 800-nm wavelength. The transmittance decreases more significantly at a shorter wavelength (~ 400 nm) for NSP-1 and NSP-2 after heat treatment, which could be due to the large-size crystal formation.

D. Indentation and fracture toughness

The mechanical properties of the as-prepared and heat-treated glass-ceramics are summarized in Table III, including Vickers hardness, crack-initiation resistance, and fracture toughness. For the as-prepared samples, the hardness at 0.49-N load is about 4.2 GPa for NSP-1, 4.5 GPa for NSP-2, and 4.6 GPa for NSP-3, respectively. After heat treatment at $1.05T_g$, the hardness changes to 3.9 GPa for NSP-1, 4.8 GPa for NSP-2, and 4.4 GPa for NSP-3. As such, hardness is not significantly affected by the increased crystallinity upon heat treatment.

Crack resistance (CR) refers to the ability of the material to resist crack initiation under the impact of a sharp object. Based on the Vickers indentation method, CR corresponds to the load when the probability of corner cracking reaches 50%. Figure 5(a) shows the curves of crack-initiation probability as a function of applied indentation load for the as-prepared and heat-treated glass-ceramics, while the determined values of CR are given in Table III. For the as-prepared samples, the crack resistance increases from 0.1 N for NSP-1 to 0.5 N for NSP-2 and 2.1 N for NSP-3. After heat treatment, the crack resistance increases to 0.4 N for NSP-1 and 0.6 N for NSP-2, respectively. However, the crack resistance of NSP-3 decreases from 2.1 to 0.3 N after heat treatment. Considering the standard deviation, heat treatment has no significant effect on the crack resistance of the NSP-1 and NSP-2 samples, whereas a decrease in the crack resistance of NSP-3 is observed. In addition, the CR results also indicate that increasing crystallinity in glass-ceramics and those containing high-content crystals tend to exhibit smaller CR .

Figures 5(b) and 5(c) show the principle of the SEPB method to obtain fracture toughness. An indented specimen

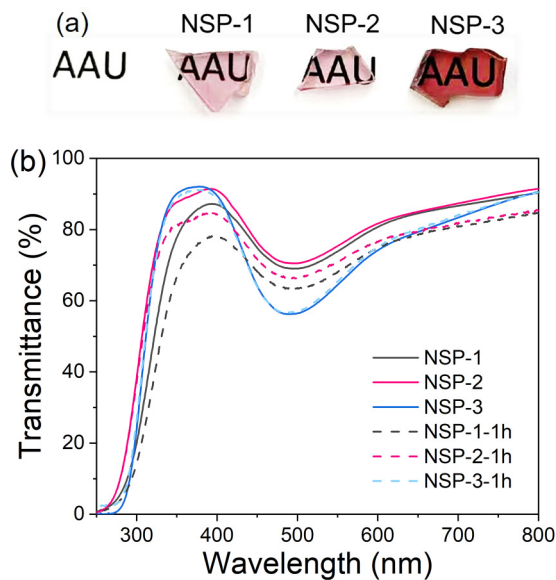


FIG. 4. (a) Photographs of polished glass-ceramics samples after heat treatment. (b) UV-vis transmittance spectra of as-prepared and heat-treated glass-ceramics.

TABLE III. Crystal average size, Vickers hardness at 0.49 N (H_V), crack resistance (CR), and fracture toughness (K_{Ic}) measured using SEPB technique of as-prepared and heat-treated glasses.

Sample ID	Crystal average size (nm)	H_V (GPa)	CR (N)	K_{Ic} [MPa m ^{0.5}]
NSP-1	47	4.2 ± 0.2	0.1 ± 0.2	0.81 ± 0.02
NSP-1-1 h	83	3.9 ± 0.1	0.4 ± 0.1	1.12 ± 0.05
NSP-2	99	4.5 ± 0.3	0.5 ± 0.1	0.72 ± 0.04
NSP-2-1 h	74	4.8 ± 0.2	0.6 ± 0.1	0.87 ± 0.05
NSP-3	44	4.6 ± 0.2	2.1 ± 0.1	0.58 ± 0.05
NSP-3-1 h	36	4.4 ± 0.2	0.3 ± 0.1	0.55 ± 0.04

was first placed into the bridge compressive fixture (precrack model) and it was ensured that the indentation line was in the middle of the groove. The length of the produced precrack was around 50% of the specimen width. Then, the precracked specimen was placed into the three-point bending fixture (fracture model) to undergo fracture. The peak load value (P_{max}) can be obtained from the load-displacement curve [shown in Fig. 5(b)], and the precrack lengths a can be calculated by the average of a_1 , a_2 , and a_3 [shown in Fig. 5(c)]. As shown in Fig. 5(d), the fracture toughness (K_{Ic}) of NSP-1 increases significantly from 0.81 to 1.12 MPa m^{0.5} upon heat treatment. Notably, the K_{Ic} of NSP-1-1h reaches a higher value among all the phosphosilicate samples. Similarly, the K_{Ic} of NSP-2 also increases from 0.72 to 0.87 MPa m^{0.5}, whereas the heat treatment has only a relatively small effect on the K_{Ic} of NSP-3, which is around 0.55 MPa m^{0.5}. In addition, based on the indentation results, we have found that the corner crack

lengths generally decrease upon heat treatment (especially for NSP-1 and NSP-2), as consistent with the general increase in the SEPB-based fracture toughness (see Supplemental Material, Fig. S4 [26]). Overall, the above results suggest that the increase in crystal size (for NSP-1) and the formation of large-sized crystals (for NSP-2) improve the fracture toughness of glass-ceramics. For NSP-3, increased crystal content appears to have a smaller effect on fracture toughness.

E. Elastic properties

Elastic moduli are listed in Table I. Young’s modulus of the glass-ceramic samples has been measured using ultrasonic thickness gauge based on the density data. For the as-prepared samples, we find Young’s modulus to be 67.2 GPa for NSP-1 and NSP-2, and 64.5 for NSP-3. Poisson’s ratio is 0.23 for NSP-1, and increases to 0.25 for NSP-2

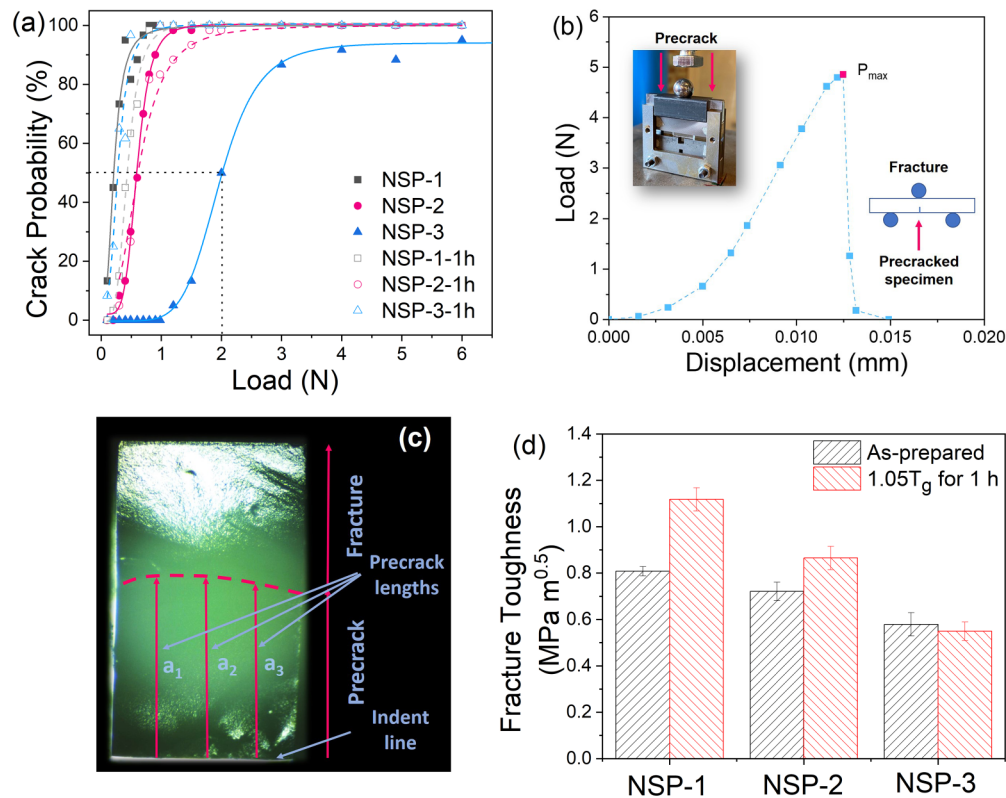


FIG. 5. (a) Crack probability as a function of applied indentation load for same samples. (b) Load-displacement curve of three-point bending of precracked SEPb specimen. Inset shows bridge-compression fixture (precrack) and three-point bending fixture with a precracked specimen (fracture). (c) Postfractured SEPb specimen. (d) Fracture toughness (K_{Ic}) for all glass-ceramics compositions and heat treatments.

and 0.26 for NSP-3. To investigate the effect of the crystal on the glass-ceramic mechanical properties, we have simulated the elastic moduli of Na_3PO_4 crystals. The simulated Young's modulus using the Voigt-Reuss-Hill (VRH) method (E_{VRH}) of crystalline Na_3PO_4 is 37.8 GPa, which is much lower than that of glass-ceramics. That is, Young's modulus of crystalline Na_3PO_4 is significantly lower than that of the residual glass matrix. The simulated bulk modulus K_{VRH} is 40.0 GPa, shear modulus G_{VRH} is 14.1 GPa, and Poisson's ratio ν is 0.34.

IV. DISCUSSION

A. Microstructure analysis

The mechanical properties of glass-ceramics are determined by their structure (glass matrix and crystals). Therefore, we first discuss the microstructure changes due to differences in chemical composition and heat treatment. Some previous work has found that when P_2O_5 is added to the $\text{Na}_2\text{O}-\text{SiO}_2$ system, the NBO-forming sodium ions from the silicate network can combine with PO_4^{3-} to form $3\text{Na}^+ \text{PO}_4^{3-}$ -like complexes and induce repolymerization in the silicate glass structure [19,20,25]. This structure facilitates the formation of Na_3PO_4 crystals, explaining why the present ^{31}P NMR results show that the Na_3PO_4 phase (i.e., $3\text{Na}^+ \text{PO}_4^{3-}$ structure) is the main phosphate structure component. More $\text{Na}_4\text{P}_2\text{O}_7$ phases form after heat treatment of the NSP-1 and NSP-3 compositions according to the ^{31}P NMR spectra. Moreover, after heat treatment, the content of the Na_3PO_4 phase increases according to the XRD result, indicating that there is still some fraction of PO_4^{3-} structures in the glass matrix. This allows two PO_4^{3-} units (together with their three charge-compensating Na^+ cations) to combine and form a $\text{Na}_4\text{P}_2\text{O}_7$ phase or similar dimer structure, and release Na^+ ions into the silicate structure [22,40]. For the NSP-2 composition, the Na_3PO_4 peak becomes sharper, which might be due to the more ordered arrangement of the sodium orthophosphate crystal phase that is formed upon heat treatment.

Aboud *et al.* have reported that in a phosphosilicate glass ($\text{SiO}_2-\text{P}_2\text{O}_5-\text{Al}_2\text{O}_3-\text{Na}_2\text{O}-\text{MgO}$), the polymeric network of the glass will be disrupted upon high-temperature or long-time heat treatment. This makes the atoms such as P or Al free to change their positions and form a common crystalline compound in the glass [51]. Other studies have also found structural depolymerization after heat treatment [52,53]. As a result, based on ^{29}Si NMR results, the Q^{n+1} can transform to Q^n in the silicate structure in glass-ceramics after heat treatment, leading to the silicate structure depolymerization for heat-treated glass-ceramics. Both effects could lead to the observed depolymerization of the glass matrix for the heat-treated glass-ceramics.

In addition, the XRD results show that the content of Na_3PO_4 crystal increases for the three heat-treated glass-ceramics, with the increase of crystallinity in NSP-3 being the most significant. However, the effect of heat treatment on the crystal size is not significant in NSP-3 [Fig. 2(c)]. Furthermore, the crystal size increases significantly from 47 to 83 nm in heat-treated NSP-1, while the effect on the crystal

size in NSP-2 by heat treatment is not pronounced, decreasing from 99 to 74 nm.

B. Effect of microstructure on transparency and mechanical properties

According to the scattering theory, the coefficient of scattering (σ) is governed by the size of crystals (R) dispersed in the glassy phase [$\sigma \propto R^3$], and the refractive-index difference between crystal (n) and glass matrix (n_0), [$\sigma \propto \{(n^2 - n_0^2)/(n^2 + n_0^2)\}^2$] [54]. Therefore, smaller-size crystals and smaller refractive-index differences provide lower scattering, which means that the glass-ceramics would have better transmittance. Most transparent glass-ceramics are achieved by the formation of crystals of small size [55]. In this work, the crystal size for glass-ceramics is above 30 nm, especially heat-treated NSP-1 and NSP-2, where the crystal size is above 50 nm. Combined with the XRD results and the observed change in crystal size, we conclude that the increases in crystal size and crystal content cause the decrease in transmittance of the glass-ceramics, especially at short wavelengths. However, although the crystal size is above 50 nm, the as-prepared and heat-treated glass-ceramics still exhibit good transmittance, which might be influenced by the similar refractive index of glass matrix and crystal. Yudar *et al.* have reported the refractive-index value of Li_3PO_4 to be approximately 1.59 [56], suggesting the refractive-index value of the Na_3PO_4 is likely around 1.5. Meanwhile, the refractive-index value of a phosphosilicate glass is also around 1.5 [54,57]. Therefore, the difference in refractive index between residual glass and Na_3PO_4 crystal is likely relatively small, which explains the excellent transmittance of the present glass-ceramics together with the size of the crystals below 100 nm. Similarly, Li *et al.* have reported good transmittance in phosphosilicate glass-ceramics with Na_3PO_4 crystals [25].

The residual glass network and crystals affect the glass-ceramic mechanical properties. Here, the simulated Young's modulus of Na_3PO_4 is around 37.8 GPa, which is much lower than that of glass-ceramics (above 60 GPa). Considering that the connectivity of the main glass matrix (silicate network) decreases after heat treatment and the Young's modulus of Na_3PO_4 crystals, this explains why the hardness of the glass-ceramics is found to decrease after heat treatment.

Next, we consider the effects of the residual glass structure and crystal on the crack resistance. For homogeneous glasses, CR depends on the indentation deformation mechanism. For example, glass compositions that are prone to densification have been reported to be more crack resistant, as it reduces the driving force (residual stresses) for cracking [28,58]. Typically, a glass with a more open structure is more prone to densification, or one with a more self-adaptive composition (such as B_2O_3 , Al_2O_3), exhibits a higher CR [4]. In addition, some reports also proposed that silicate glasses with highly cross-linked rigid networks tend to exhibit lower CR [59,60]. In the present samples, there are no self-adaptive components, while the glass-ceramic with higher NBOs content decreases the rigidity of the network, which could increase the crack resistance. That would be one reason to explain why the NSP-3 exhibits the highest CR . On the other hand, upon heat treatment, the high residual stresses will be generated

inside the glass-ceramics due to the mismatch of the coefficient of thermal expansion (CTE) between the crystalline and glassy phases, which could decrease the crack resistance [10], as residual stress is the driving force for cracking in oxide glass [4]. Some papers have reported that the CTE of sodium phosphosilicate glass is around $13 \times 10^{-6} \text{ K}^{-1}$ and the CTE of glass-ceramics with Na_3PO_4 crystal increases to $16 \times 10^{-6} \text{ K}^{-1}$ [11,25]. Residual stresses arise in glass-ceramics by cooling the sample from high temperatures due to CTE differences between the precipitates and the glass matrix [11,61]. Following Eq. (6), higher residual stress is generated in glass-ceramics with higher-volume fractions of crystals or large differences in CTE [11],

$$\sigma_p = \frac{\Delta\alpha \Delta T}{\frac{1}{3K_p} + \frac{1}{4(1-f)G_m} + \frac{1}{3(1-f)K_m}}. \quad (6)$$

Here, σ is the residual stress, G is the shear modulus, K is the bulk modulus, and f is the volume fraction of precipitates. The subscripts m and p refer to matrix and particle, respectively. $\Delta\alpha$ is the difference between the linear thermal expansion of the precipitate and the matrix, and ΔT is the difference between T_g (when the glass stops flowing on cooling) and room temperature. When the thermal expansion of the crystalline phase is higher than that of glass matrix, homogeneous tensile stress developed. Hence, in this work, the higher the crystal content, the more residual stress is present in the glass-ceramics, which could lead to easier crack initiation. Considering the lowest crystallinity and highest NBOs content in NSP-3, the NSP-3 exhibits the best crack resistance among the three as-prepared glass-ceramics.

After heat treatment, the crystallinity of all samples increases, especially in the case of the NSP-3 composition. The residual stress in NSP-3-1h is much greater than that in the as-prepared NSP-3, and therefore the CR is significantly reduced. However, the NBO/T of heat-treated samples is higher compared to the as-prepared samples, indicating that the connectivity of the silicate network decreases, which could lead to an increase in crack resistance of heat-treated glass-ceramics [59,60]. Thus, the crack resistance of NSP-2 and NSP-3 samples increases slightly upon heat treatment. In conclusion, crystallinity plays a major role in affecting crack resistance for glass-ceramics with an obvious increase in crystallinity. For samples with little change in crystallinity, the glass network plays a more important role. Finally, although the crystal size in NSP-1 increases significantly after heat treatment, there is no apparent effect on the crack resistance.

For homogeneous glasses, K_{Ic} is sensitive to the network connectivity, since less cross-linked networks display less resistance to crack propagation on account of their lower cohesion [16,62]. For glass-ceramics, the heterogeneous microstructure can effectively dissipate the high local stresses through crack deflection, multiple cracking, crack bridging, and crack branching operated at the crack tip, which can lead to improved fracture toughness [63–65]. Peitl *et al.* have reported that glass-ceramics with a highly crystallized volume fraction or relatively large crystal size usually exhibit better fracture toughness [11,63]. In this work, the K_{Ic} of as-prepared glass-ceramic decreases from NSP-1 to NSP-3, since the NBO/T of the residual glass phase decreases, i.e., the lower

connectivity of the silicate network reduces the resistance to crack propagation. From the crystal impact perspective, the crystallinity of NSP-1 and NSP-2 is higher than that of NSP-3; thus, the effect of crack deflection or crack pinning in NSP-1 and NSP-2 is more obvious than in NSP-3. As a result, the K_{Ic} of NSP-1 is higher than that of NSP-2, and the K_{Ic} of NSP-3 is the lowest.

After heat treatment, NBO/T is increased compared to the as-prepared glass-ceramics. The depolymerization of the glass network means the residual glass in the heat-treated glass-ceramics is less resistant to crack propagation. However, the crystallinity of heat-treated glass-ceramics increases compared to the as-prepared samples, which would improve the fracture toughness. Therefore, the residual glass and crystallization compete in the influence on K_{Ic} . Furthermore, the residual stress would also play a role since the mismatch in CTE puts the glass matrix in a local state of tension. Although the increase in crystallinity of NSP-1 is relatively smaller compared to that of NSP-3 after heat treatment, the crystal size in NSP-1 increases significantly from 47 to 83 nm. Therefore, the K_{Ic} is greatly improved from 0.81 to $1.12 \text{ MPa m}^{0.5}$ (i.e., a relative increase of 38%). This indicates a more important effect of crystals on fracture toughness relative to the effect of the residual glass-network structure. However, although the increase in crystallinity of heat-treated NSP-3 is more significant than that of the other two heat-treated samples, the crystal size and K_{Ic} did not increase. This indicates that the improved fracture toughness caused by the increased crystallinity is offset by the weakening of the residual glass-network depolymerization. For NSP-2, the increase of crystallinity in NSP-2-1h is the smallest among the compositions, but the crystal size is the largest. Therefore, the increase in K_{Ic} of NSP-2-1h is still significant compared to NSP-3-1h, with an increase from 0.72 to $0.87 \text{ MPa m}^{0.5}$ (i.e., a relative increase of 21%). Unfortunately, it is challenging to conclude on crack path directly based on the SEM images, i.e., whether the cracks are passing through or circumventing the particles, due to the small crystal size. However, the overall analysis of the results demonstrates that the increase in crystallinity and crystal size improves the fracture toughness of the glass-ceramics, with the crystal size (or the increase of large-sized crystals content) having the most prominent effect. Notably, the maximum fracture toughness of $1.1 \text{ MPa m}^{0.5}$ is significantly higher than that of both soda-lime silica as well as $\text{Na}_2\text{O}-\text{CaO}-\text{SiO}_2-\text{P}_2\text{O}_5$ glasses (both around $0.7 \text{ MPa m}^{0.5}$) [6,11].

V. CONCLUSION

In this work, we have prepared transparent sodium phosphosilicate glass-ceramics with nanocrystals and investigated the relationship between structure (crystal and residual glass structure) and mechanical properties. After heat treatment, the fraction of nonbridging oxygens increases, indicating that the network connectivity of the residual glass matrix decreases, but it also induces the formation of Na_3PO_4 crystals. Specifically, the crystallinity of the NSP-3 sample increases significantly after the heat treatment, but the crystal size does not significantly change. On the other hand, heat treatment induces a significant increase in the crystal size of the NSP-1

sample (from 47 to 83 nm), but a minor increase in crystallinity. For NSP-2, the crystallinity and crystal size are not significantly influenced by the heat treatment.

The structure of the residual glass phase and the content and size of the crystals all have different effects on mechanical properties of the glass-ceramics. The depolymerization of the residual glass network increases the resistance to crack initiation but reduces the resistance to crack propagation. One interesting finding is that the increase in crystal content leads to crack initiation, i.e., the glass-ceramics with higher crystallinity tend to exhibit lower crack resistance, whereas changes in the crystal size do not appear to have an effect on crack resistance. Although the fracture toughness of glass-ceramic with higher crystallinity is larger, the increase in crystal size or the formation of larger-size crystals is more effective in improving the fracture toughness of glass-ceramics. All the investigated glass-ceramic samples feature excellent transmittance, reaching a maximum fracture tough-

ness of 1.1 MPa m^{0.5}. This study thus provides guidelines for developing high-toughness, yet transparent, glass-ceramics. For example, such nanoglass-ceramics could potentially be used as rare-earth doped materials for photonic applications with good mechanical properties.

ACKNOWLEDGMENTS

We acknowledge the financial support from the European Union's Horizon 2020 research and innovation programme under the Marie Skłodowska-Curie Grant Agreement No. 882520. M.B. acknowledges funding from the National Science Foundation under the Grants No. DMR-1944510, No. DMR-1928538, and No. CMMI-1762292. F.M. acknowledges funding from Agencia Estatal de Investigación of Spain through Project No. PID2020-115419GB-C21/AEI/10.13039/501100011033.

-
- [1] L. Wondraczek, J. C. Mauro, J. Eckert, U. Kühn, J. Horbach, J. Deubener, and T. Rouxel *Advanced Materials* **23**, 4578 (2011).
- [2] X. Chen, Y. Tian, W. Hu, P. Lu, B. Tan, F. Chen, and Y. Zhang, *Ceram. Int.* **45**, 24878 (2019).
- [3] G. A. Rosales-Sosa, A. Masuno, Y. Higo, and H. Inoue, *Sci. Rep.* **6**, 23620 (2016).
- [4] K. Januchta, R. E. Youngman, A. Goel, M. Bauchy, S. L. Logunov, S. J. Rzoska, M. Bockowski, L. R. Jensen, and M. M. Smedskjaer, *Chem. Mater.* **29**, 5865 (2017).
- [5] J. Sehgal and S. Ito, *J. Am. Ceram. Soc.* **81**, 2485 (1998).
- [6] T. Rouxel and S. Yoshida, *J. Am. Ceram. Soc.* **100**, 4374 (2017).
- [7] J. Lewandowski, M. Shazly, and A. S. Nouri, *Scr. Mater.* **54**, 337 (2006).
- [8] D. Tulyaganov, S. Agathopoulos, J. Ventura, M. Karakassides, O. Fabrichnaya, and J. Ferreira, *J. Eur. Ceram. Soc.* **26**, 1463 (2006).
- [9] D. Li, J. Guo, X. Wang, S. Zhang, and L. He, *Mater. Sci. Eng.: A* **669**, 332 (2016).
- [10] X. Ke, Z. Shan, Z. Li, Y. Tao, Y. Yue, and H. Tao, *J. Am. Ceram. Soc.* **103**, 3600 (2020).
- [11] O. Peitl, E. D. Zanotto, F. C. Serbena, and L. L. Hench, *Acta Biomater.* **8**, 321 (2012).
- [12] J. Quinn, V. Sundar, and I. K. Lloyd, *Dent. Mater.* **19**, 603 (2003).
- [13] B. Deng, J. Luo, J. T. Harris, C. M. Smith, and M. E. McKenzie, *Scr. Mater.* **162**, 277 (2019).
- [14] W. Shi and P. James, *J. Mater. Sci.* **29**, 824 (1994).
- [15] P. Liu, K. Januchta, L. R. Jensen, M. Bauchy, and M. M. Smedskjaer, *J. Am. Ceram. Soc.* **103**, 944 (2020).
- [16] K. Januchta, T. To, M. S. Bødker, T. Rouxel, and M. M. Smedskjaer, *J. Am. Ceram. Soc.* **102**, 4520 (2019).
- [17] Z. Li, C. Chen, W. Shen, D. Zhou, L. R. Jensen, X. Qiao, J. Ren, J. Du, Y. Zhang, J. Qiu, and Y. Yue, *Adv. Opt. Mater.* **10**, 2102713 (2022).
- [18] L. Martel, M. Allix, F. Millot, V. Sarou-Kanian, E. Véron, S. Ory, D. Massiot, and M. Deschamps, *J. Phys. Chem. C* **115**, 18935 (2011).
- [19] A. Tilocca and A. N. Cormack, *J. Phys. Chem. B* **111**, 14256 (2007).
- [20] M. Mirsaneh, I. M. Reaney, P. V. Hatton, S. Bhakta, and P. F. James, *J. Non-Cryst. Solids* **354**, 3362 (2008).
- [21] F. Muñoz, L. Montagne, L. Delevoye, A. Durán, L. Pascual, S. Cristol, and J.-F. Paul, *J. Non-Cryst. Solids* **352**, 2958 (2006).
- [22] H. Grussaute, L. Montagne, G. Palavit, and J. Bernard, *J. Non-Cryst. Solids* **263**, 312 (2000).
- [23] S. Xu, H. Zhang, B. Qiao, and Y. Wang, *Cryst. Growth Des.* **21**, 7306 (2021).
- [24] S. Liu, S. Lan, H. Tao, and Y. Yue, *J. Eur. Ceram. Soc.* **39**, 3876 (2019).
- [25] J. Li, M. Wang, and P. Lu, *J. Am. Ceram. Soc.* **104**, 5614 (2021).
- [26] See Supplemental Material at <http://link.aps.org/supplemental/10.1103/PhysRevMaterials.7.063606> for details of glass chemical compositions, ultrasonic echography measurements, average change in the calculated stress in the tensile and shear directions, SEM morphology and crystal-size distribution, DSC heating curves, and indentation crack length and SEP-based fracture toughness of the samples.
- [27] D. Massiot, F. Fayon, M. Capron, I. King, S. Le Calvé, B. Alonso, J. O. Durand, B. Bujoli, Z. Gan, and G. Hoatson, *Magn. Reson. Chem.* **40**, 70 (2002).
- [28] P. Liu, A. L. Søndergaard, R. E. Youngman, S. J. Rzoska, M. Bockowski, L. R. Jensen, and M. M. Smedskjaer, *J. Am. Ceram. Soc.* **104**, 1345 (2021).
- [29] M. Wada, H. Furukawa, and K. Fujita, in *Proceedings of International Congress Glass* (Ceramic Society of Japan, Kyoto, 1974), p. 39.
- [30] T. To, S. S. Sørensen, J. F. Christensen, R. Christensen, L. R. Jensen, M. Bockowski, M. Bauchy, and M. M. Smedskjaer, *ACS Appl. Mater. Interfaces* **13**, 17753 (2021).
- [31] T. To, S. S. Sørensen, M. Stepniewska, A. Qiao, L. R. Jensen, M. Bauchy, Y. Yue, and M. M. Smedskjaer, *Nat. Commun.* **11**, 2593 (2020).
- [32] T. To, F. Célarié, C. Roux-Langlois, A. Bazin, Y. Gueguen, H. Orain, M. Le Fur, V. Burgaud, and T. Rouxel, *Acta Mater.* **146**, 1 (2018).

- [33] T. To, F. Célarié, Y. Gueguen, C. Lim, R. Horm, V. Burgaud, M. Le Fur, J. Chollet, H. Orain, and T. Rouxel, *J. Non-Cryst. Solids* **566**, 120873 (2021).
- [34] M. Bertani, M. C. Menziani, and A. Pedone, *Phys. Rev. Mater.* **5**, 045602 (2021).
- [35] A. Pedone, G. Malavasi, M. C. Menziani, A. N. Cormack, and U. Segre, *J. Phys. Chem. B* **110**, 11780 (2006).
- [36] R. J. Harrison, A. Putnis, and W. Kockelmann, *Phys. Chem. Chem. Phys.* **4**, 3252 (2002).
- [37] R. Hill, *Proc. Phys. Soc. London, Sect. A* **65**, 349 (1952).
- [38] T. Duncan and D. Douglas, *Chem. Phys.* **87**, 339 (1984).
- [39] M. J. Toplis and T. Schaller, *J. Non-Cryst. Solids* **224**, 57 (1998).
- [40] C. Mercier, C. Follet-Houttemane, A. Pardini, and B. Revel, *J. Non-Cryst. Solids* **357**, 3901 (2011).
- [41] I. Mudrakovskii, V. Shmachkova, N. Kotsarenko, and V. Mastikhin, *J. Phys. Chem. Solids* **47**, 335 (1986).
- [42] S. Hayashi and K. Hayamizu, *Bull. Chem. Soc. Jpn.* **62**, 3061 (1989).
- [43] J. Stevels, *J. Soc. Glass Technol.* **30**, 64 (1946).
- [44] H. Aguiar, E. Solla, J. Serra, P. González, B. León, F. Malz, and C. Jäger, *J. Non-Cryst. Solids* **354**, 5004 (2008).
- [45] A. Silva, C. Queiroz, S. Agathopoulos, R. Correia, M. Fernandes, and J. Oliveira, *J. Mol. Struct.* **986**, 16 (2011).
- [46] H. Yamashita, H. Yoshino, K. Nagata, I. Yamaguchi, M. Ookawa, and T. Maekawa, *J. Ceram. Soc. Jpn.* **106**, 539 (1998).
- [47] H. Yamashita, K. Nagata, H. Yoshino, K. Ono, and T. Maekawa, *J. Non-Cryst. Solids* **248**, 115 (1999).
- [48] D. Miyabe, M. Takahashi, Y. Tokuda, T. Yoko, and T. Uchino, *Phys. Rev. B* **71**, 172202 (2005).
- [49] Q. Zhang, H. Yang, F. Zeng, S. Wang, D. Tang, and T. Zhang, *RSC Adv.* **5**, 41772 (2015).
- [50] A. Gaddam, H. R. Fernandes, D. U. Tulyaganov, M. J. Pascual, and J. M. Ferreira, *RSC Adv.* **4**, 13581 (2014).
- [51] T. Aboud and L. Stoch, *J. Non-Cryst. Solids* **219**, 149 (1997).
- [52] Y. Zhang, H. Li, S. Liu, N. Wu, and S. OuYang, *J. Non-Cryst. Solids* **563**, 120701 (2021).
- [53] R. Karan, P. Pal, P. Maiti, and K. Das, *J. Non-Cryst. Solids* **556**, 120554 (2021).
- [54] S. Morimoto, *J. Non-Cryst. Solids* **352**, 756 (2006).
- [55] K. Shioya, T. Komatsu, H. G. Kim, R. Sato, and K. Matusita, *J. Non-Cryst. Solids* **189**, 16 (1995).
- [56] H. H. Yudar, S. Pat, Ş. Korkmaz, S. Özen, and Z. Pat, *J. Mater. Sci. Mater. Electron.* **28**, 14499 (2017).
- [57] S. Y. Marzouk and M. Azooz, *Silicon* **4**, 157 (2012).
- [58] K. Januchta, M. Bauchy, R. E. Youngman, S. J. Rzoska, M. Bockowski, and M. M. Smedskjaer, *Phys. Rev. Mater.* **1**, 063603 (2017).
- [59] K. Januchta, P. Liu, S. R. Hansen, T. To, and M. M. Smedskjaer, *J. Am. Ceram. Soc.* **103**, 1656 (2020).
- [60] T. K. Bechgaard, A. Goel, R. E. Youngman, J. C. Mauro, S. J. Rzoska, M. Bockowski, L. R. Jensen, and M. M. Smedskjaer, *J. Non-Cryst. Solids* **441**, 49 (2016).
- [61] V. R. Mastelaro and E. D. Zanotto, *J. Non-Cryst. Solids* **194**, 297 (1996).
- [62] R. J. Eagan and J. Swearengen, *J. Am. Ceram. Soc.* **61**, 27 (1978).
- [63] Q. Fu, E. M. Aaldenberg, E. N. Coon, T. M. Gross, A. M. Whittier, B. M. Abel, and D. E. Baker, *Adv. Eng. Mater.* **24**, 2200350 (2022).
- [64] K. Maeda, K. Iwasaki, S. Urata, K. Akatsuka, and A. Yasumori, *J. Am. Ceram. Soc.* **102**, 5535 (2019).
- [65] M. Chen, S. Zhu, M. Shen, F. Wang, and Y. Niu, *Mater. Sci. Eng.: A* **528**, 1360 (2011).